Article:
Zoccarato, C., Baù, D., Bottazzi, F. et al. (4 more authors) (2016) On the importance of the heterogeneity assumption in the characterization of reservoir geomechanical properties. Geophysical Journal International, 207 (1). pp. 47-58. ISSN 0956-540X

https://doi.org/10.1093/gji/ggw259

Published on *Geophys. J. Int.*, October 2016, 207 (1): 47-58, doi: 10.1093/gji/ggw259. First published online July 13, 2016

On the importance of the heterogeneity assumption in the characterization of reservoir geomechanical properties

C. Zoccarato[1], D. Baù[2], F. Bottazzi[3], M. Ferronato[1], G. Gambolati[1], *S. Mantica*[3], *& P. Teatini*[1]

[1] *Dept. of Civil, Architectural and Environmental Engineering, University of Padova, Padova, Italy*

[2] *Dept. of Civil and Structural Engineering, The University of Sheffield, Sheffield, UK*

[3] *Development, Operations and Technology, eni S.p.A., San Donato Milanese, Italy*

SUMMARY

The geomechanical analysis of a highly compartmentalized reservoir is performed to simulate the seafloor subsidence due to gas production. The available observations over the hydrocarbon reservoir consist of bathymetric surveys carried out before and at the end of a ten-year production life. The main goal is the calibration of the reservoir compressibility c_M, i.e., the main geomechanical parameter controlling the surface response. Two conceptual models are considered: in one (a) c_M varies only with the depth and the vertical effective stress (heterogeneity due to lithostratigrafic variability); in another (b) c_M varies also in the horizontal plane, that is, it is spatially distributed within the reservoir stratigraphic units. The latter hypothesis accounts for a possible partitioning of the reservoir due to the presence of sealing faults and thrusts that suggests the idea of a block heterogeneous system with the number of reservoir blocks equal to the number of uncertain parameters. The method applied here relies on an ensemble-based data assimilation (DA) algorithm (i.e., the Ensemble Smoother, ES), which incorporates the information from the bathymetric measurements into the geomechanical model response to infer and reduce the

uncertainty of the parameter c_M. The outcome from conceptual model (a) indicates that DA is effective in reducing the c_M uncertainty. However, the maximum settlement still remains underestimated, while the areal extent of the subsidence bowl is overestimated. We demonstrate that the selection of the heterogeneous conceptual model (b) allows to reproduce much better the observations thus removing a clear bias of the model structure. DA allows significantly reducing the c_M uncertainty in the five blocks (out of the seven) characterized by large volume and large pressure decline. Conversely, land subsidence can constrain only partially the partitions that marginally contributes to the cumulative displacements of the seafloor.

Key words: geomechanics – parameters identification – seafloor subsidence – heterogeneity – compartmentalized reservoirs

1 INTRODUCTION

The prediction of the subsurface compaction of producing hydrocarbon fields is an important issue within the general reservoir management framework. Undesirable impacts such as casing deformations and wellbore failures (Hilbert et al. 1999; Fredrich et al. 2000; Sayers et al. 2006) must be prevented to reduce significant economical risks and ensure the maximum safety of the drilling operations. Moreover, the forecast of the land subsidence caused by the compaction of the rock formation can be of major importance. Indeed, the surface settlement can cause, in the case of offshore reservoirs, platform sinking, as observed at the Ekofisk field in the North Sea (Kristiansen & Plischke 2010), pipeline deformation and a certain environmental impact particularly in coastal areas (Morton et al. 2006; Baù et al. 2000; De Waal 2012).

Geomechanical simulators have long been recognised as important tools to predict land subsidence during and after field operations, as well as to evaluate the risks associated with it. However, numerical modelling of the reservoir geomechanical response to fluid extraction is affected by several sources of uncertainty, such as the rock mechanical properties, the geological structure of the reservoir, and the initial stress regime. In light of the above, establishing a probabilistic framework may provide a powerful strategy to cope with the problem uncertainties and to constrain our knowledge of the system.

The major geomechanical parameter influencing rock compaction is the vertical uniaxial rock compressibility c_M (van Hasselt 1992; Baù et al. 2002; Hueckel et al. 2005). An overview of the methodologies used to estimate c_M is given in Ferronato et al. (2004, 2013). This parameter can be

evaluated from either laboratoy tests or *in situ* field investigations. In the former category, core samples are tested in compaction devices, which aim at replicating the loading conditions expected in the reservoir. Most often, these conditions are hard to reproduce in the laboratory, which can result in significant errors of estimation of the reservoir rock properties. As to the latter category, the radioactive-marker technique (RMT) was developed in the 1990s and 2000s to estimate rock properties based on direct measurements of the reservoir compaction (Cassiani & Zoccatelli 2000; Baù et al. 2002; Kristiansen & Plischke 2010). With the RMT, the reservoir compaction is measured by monitoring the variation of the vertical distance between a series of isotope markers shot into the formation through logging boreholes. Despite the improved results with respect to laboratory techniques, the interpretation of RMT data remains affected by uncertainties and caution to their use is recommendable (Ferronato et al. 2003, 2004). For example, radioactive markers need to be installed in non-producing wellbores, as the presence of a horizontal pressure gradient may lead to underestimating c_M. In addition, a detailed knowledge of the reservoir lithostratigraphy is needed to optimally position the radioactive markers and correctly interpret the corresponding measurements.

Values of c_M can be also "inverted" using observations of ground movement obtained, for example, with satellite Interferometric Synthetic Aperture Radar (InSAR) measurements (Ferronato et al. 2013). Teatini et al. (2011) used these type of measurements to calibrate a finite element (FE) transversely isotropic model to simulate the behaviour of an underground gas storage (UGS) reservoir in Italy. The methodology provided an indirect estimate of the c_M in loading/reloading conditions. Moreover, 4D seismic data, that is, time-lapse 3D seismic surveys, can be used as indirect information for the prediction of reservoir petrophysical properties (Mezghani et al. 2004; Hatchell & Bourne 2005; Herwanger & Horne 2009).

Since each of the measurement methods presented above is affected by uncertainties, it is advisable to select data with caution and develop procedures to integrate different and seemingly independent sources of information, as well as validate simulation results. In this work, we apply a data assimilation (DA) framework to infer the reservoir rock compressibility c_M and reduce the uncertainties in its estimation. DA is an analysis technique that allows for incorporating observations from a dynamical system into a simulation model solution to reduce the uncertainty in the forecast of the system state. In reservoir history-matching applications, DA has been used to update the dependent variables of multiphase flow models, such as pressure and saturations, and as an inverse modelling tool to "condition" model parameters, such as porosity and permeability, based on the observed data (e.g. Lorentzen et al. 2003, Nævdal et al. 2003, Gu & Oliver 2005, Skjervheim et al. 2011, Emerick & Reynolds 2013).

The estimation of geomechanical parameters via DA is a fairly new application. Fokker et al.

(2013) employed measurements of ascending and descending line-of-sight displacements from InSAR to calibrate the compaction coefficient and the subsurface basement elastic modulus for the Bergermeer gas field in the Netherlands. Baù et al. (2014) presented an Ensemble Smoother (ES), i.e., an ensemble-based DA approach, to joint assimilate horizontal and vertical land surface displacements into a hypothetical reservoir model based on Geertsma's analytical solution (Geertsma 1973). A real-world application is presented by Zoccarato et al. (2016), in which the ES is used to reduce the uncertainty on the constitutive parameters characterizing a transversely isotropic geomechanical model of a UGS reservoir. The calibrated parameters are homogeneously distributed in the domain, although the heterogeneity due to the lithostratigrafic variability according to the dependency of c_M on the depth, z, and the vertical effective stress, σ_z is properly accounted for.

In this study, an ES parameter estimation technique is developed and implemented using seafloor bathymetric observations, collected over an offshore gas reservoir, the *Maja* field. Two conceptual models for c_M are selected and compared. As in Zoccarato et al. (2016), the first conceptual model assumes c_M dependent on z and σ_z on account of a basin-scale variability due to lithostatic loading. In the second conceptual model, c_M varies not only with respect to z and σ_z, but also horizontally, that is, it is assumed to be spatially distributed within the reservoir layers. This assumption is justified by the strong compartmentalization of the *Maja* reservoir, which is physically partitioned into separate blocks, or zones, by a complex system of faults and thrusts. To our knowledge, this is the first attempt to calibrate c_M as a three-dimensional field.

The constitutive law of c_M versus σ_z is assumed to be known from previous basin-scale characterizations from RMT surveys (Baù et al. 2002; Ferronato et al. 2013). The horizontal heterogeneity is introduced into the model by means of a horizontally varying function $f_{c_M}(x, y)$, which multiplies the $c_M(\sigma_z)$ constitutive law. Note that we do not aim to derive a new basin-scale compressibility relationship, but rather to infer local (at the scale of the reservoir) heterogeneities of c_M by inverting surface displacement observations.

This paper is organized as follows. Section 2 describes the major components of the methodology followed in this work. These consist of the reservoir dataset available for the *Maja* gas field, the geomechanical model, the available observations of surface displacements, and the ES algorithm used to estimate the geomechanical model parameters. Section 2 also gives a detailed description of the two conceptual models used for represent the heterogeneity of the c_M field. The results of the numerical forecast and the application of the inversion algorithm are presented in Section 3, along with a discussion (Section 4) on the adequacy of the adopted conceptual models. The conclusions that can be drawn from this work are summarized in Section 5.

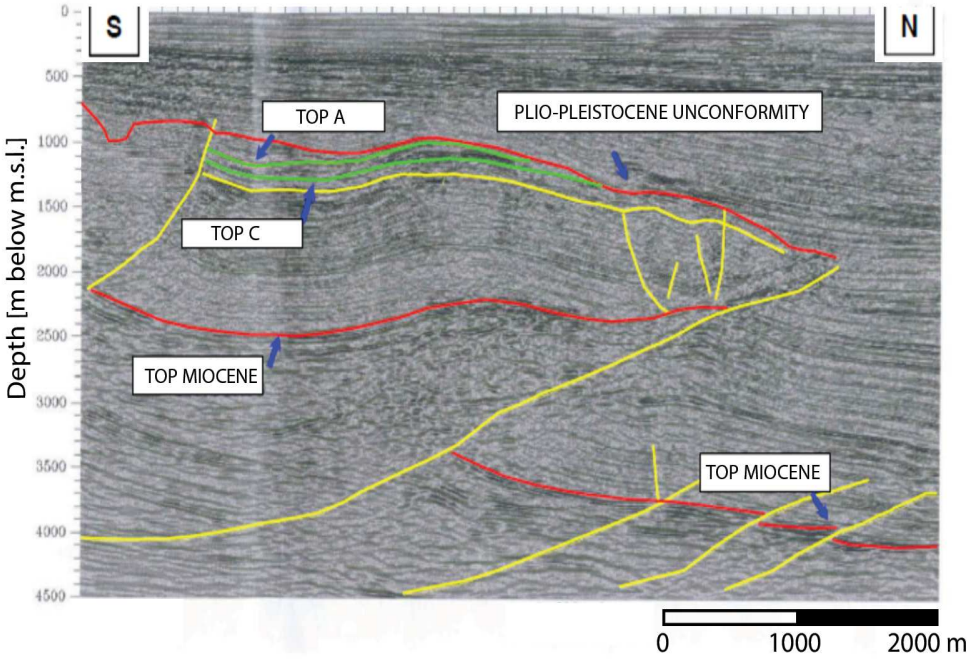

Figure 1. South-North interpreted seismic section through the *Maja* reservoir.

2 METHODOLOGY

Our approach relies on the combination of a reservoir geomechanical model, data of surface displacements observed over the *Maja* reservoir and a DA framework that merges the latter into the results of the former. These elements are presented in the following.

2.1 The *Maja* Gas Field

The *Maja* field is an offshore gas reservoir that was developed over a period of ten years starting in the late 1990s. The field location cannot be published to comply with a confidentiality agreement made with the operator managing the gas field. Gas was produced from three main gas pools A, B, and C hydraulically disconnected from one another (Fig.1). The fluid pore pressure distribution in these layers is obtained with the reservoir multiphase simulator $ECLIPSE^{TM}$ through history matching of the measured wellbore fluid pressures and gas production rates. Maps of the pressure change, ΔP, at the end of the ten-years production life of the reservoir are shown in Fig.2(b-d). The gas bearing pools are subdivided into different compartments delimited by sealing faults and/or thrusts as shown in the schematic representation of the fault-block distribution of Fig. 2a. The reservoir compartmentalization is derived from 3D seismic survey and accordingly supported by the pressure change in the geologic blocks measured during the field production.

The largest ΔP reached -75 bar in the intermediate pool B (Fig.2c) at the end of the field produc-

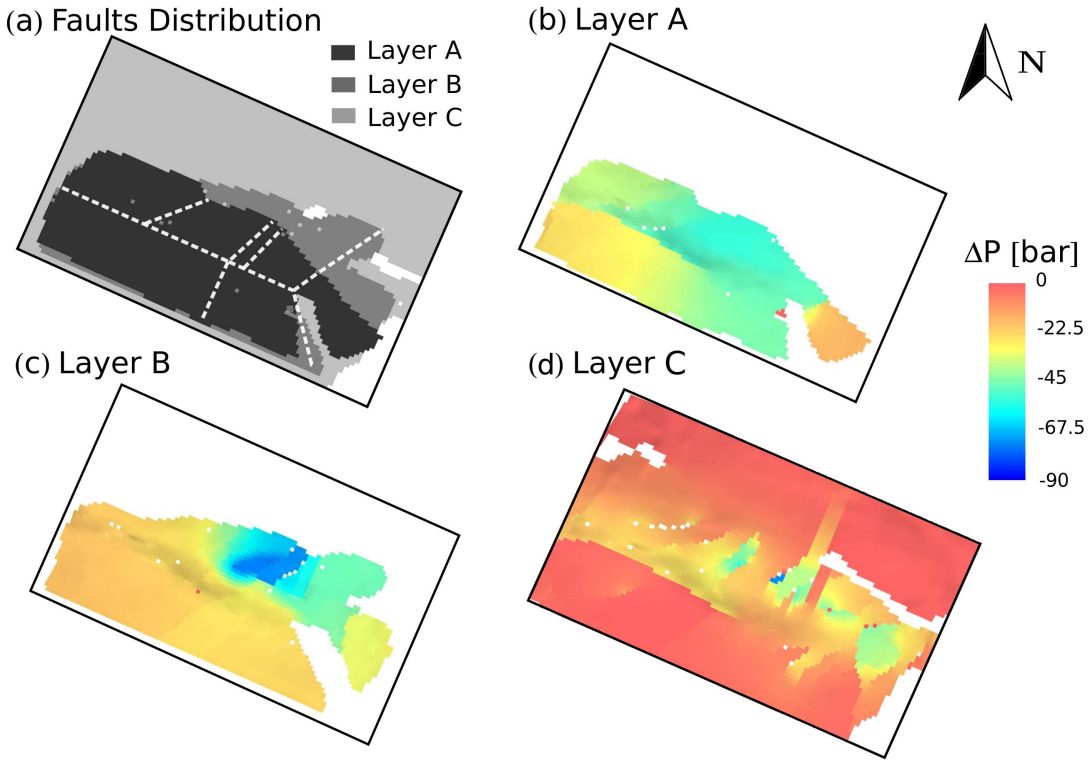

Figure 2. (a) Schematic representation of the fault-block distribution within the *Maja* gas reservoir and (b)-(d) maps of the pressure change ΔP occurring in layer A, B, and C. The pore pressure variation is experienced over ten years of production.

tion. The aquifer hydraulically connected with pool B is significantly compartmentalized and divided into three blocks with an average ΔP $\sim$ -20 bar, -45 bar, and -30 bar. Pool A shows a different pressure distribution with ΔP varying from a -45 bar to -18 bar. Negligible ΔP is found in the deeper gas pool C except for the central blocks.

The reservoir porosity ϕ varies from 15% to 29%. In pools A and B, the horizontal permeability k_h ranges from 30 to 250 mD and from 13 to 680 mD, respectively. In pool C, k_h equals 13 mD. The vertical permeability k_v is $0.1k_h$.

2.2 Reservoir Geomechanics

The subsurface deformation is a major consequence of the pore pressure change in space and time due to the injection or the extraction of fluids. The numerical solution of the governing flow and the structural partial differential equations (PDEs) is required to simulate the deformation up to the land surface. With the so-called “one-way” coupling approach, the fluid pore pressure variation obtained with a reservoir multiphase flow simulation is used as forcing term in a geomechanical model to

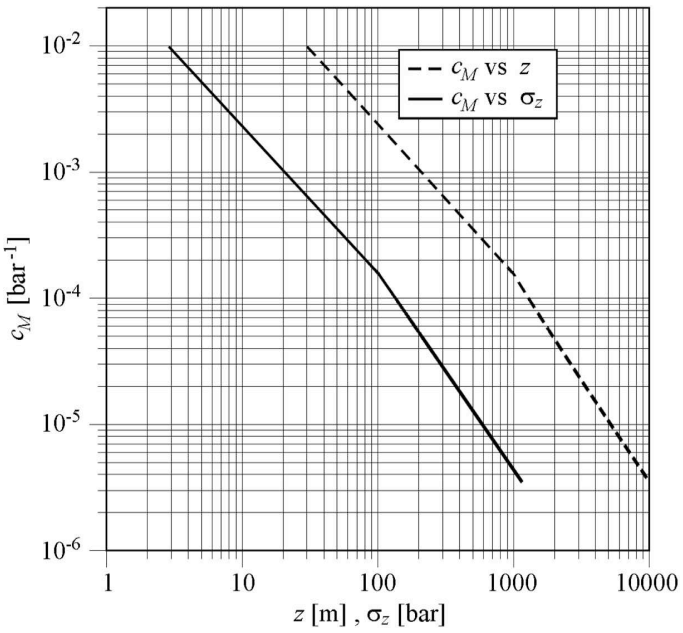

Figure 3. Scale basin constitutive laws, c_M vs. z and c_M vs. σ_z for the *Maja* gas field (modified after Baù et al. (2002)).

simulate the ensuing surface motion. In this work, the geomechanical behavior of the reservoir is simulated using a FE poro-elasto-plastic model (Gambolati et al. 2001; Janna et al. 2012). The isotropic relationship between the incremental effective stress $\boldsymbol{\sigma}$ and strain $\boldsymbol{\epsilon}$ vectors reads:

$$d\boldsymbol{\epsilon} = \boldsymbol{C} d\boldsymbol{\sigma} \Rightarrow \begin{Bmatrix} d\epsilon_{xx} \\ d\epsilon_{yy} \\ d\epsilon_{zz} \\ d\gamma_{xy} \\ d\gamma_{yz} \\ d\gamma_{zx} \end{Bmatrix} = \begin{bmatrix} \frac{1}{E} & -\frac{\nu}{E} & -\frac{\nu}{E} & 0 & 0 & 0 \\ \frac{\nu}{E} & \frac{1}{E} & -\frac{\nu_v}{E} & 0 & 0 & 0 \\ -\frac{\nu}{E} & -\frac{\nu}{E} & \frac{1}{E} & 0 & 0 & 0 \\ 0 & 0 & 0 & \frac{2(1+\nu)}{E} & 0 & 0 \\ 0 & 0 & 0 & 0 & \frac{2(1+\nu)}{E} & 0 \\ 0 & 0 & 0 & 0 & 0 & \frac{2(1+\nu)}{E} \end{bmatrix} \begin{Bmatrix} d\sigma_{xx} \\ d\sigma_{yy} \\ d\sigma_{zz} \\ d\tau_{xy} \\ d\tau_{yz} \\ d\tau_{zx} \end{Bmatrix} \tag{1}$$

where E and ν are the Young and Poisson moduli, respectively. E and ν are linked to the vertical uniaxial compressibility c_M through the well known relationship $c_M = [(1+\nu)(1-2\nu)]/[E(1-\nu)]$.

For the *Maja* gas field, c_M varies accordingly with the hypo-plastic relationship developed by Baù et al. (2002) and improved by Ferronato et al. (2013). This model is described in Fig. 3. Initially, that is, before the field development, c_M is distributed depending exclusively on the depth z. Depth and vertical effective stress σ_z are linked through the Terzaghi relationship $\sigma_z(z) = ovb(z) \cdot z - p(z)$ where $ovb(z)$ is the overburden gradient derived from density log and $p(z)$ is the initial fluid pressure. During production c_M varies with σ_z, which is increased due to the reduction of fluid pressure associated with gas production from the reservoir.

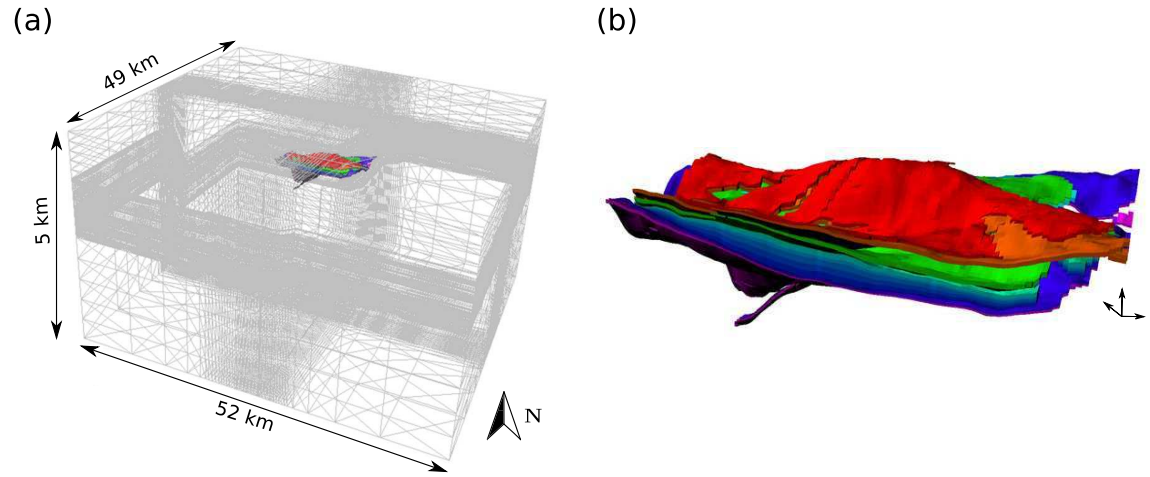

Figure 4. (a) Axonometric view of the 3D Finite Element (FE) grid of the geomechanical model of the *Maja* gas field with the colored elements corresponding to the productive units of the (b) reservoir production model. The colors in (b) are representative of the reservoir layers.

Fig. 4 depicts the three dimensional grid used to discretize the geological setting in which the *Maja* reservoir is embedded. This grid is made up by 320,901 nodes and 1,824,768 tetrahedral elements and covers a domain of 52 km×49 km×5 km (Fig. 4a). Reservoir layers in pools A, B, and C (Fig. 4b), which are subject to pressure variation, include a total of 54,720 elements. No-displacement conditions are prescribed on the lateral and bottom boundaries of the domain, whereas its top, that is, the seafloor, is assumed traction-free.

2.3 Bathymetric survey data

The bathymetry is the measurement of the depth of a water body, corresponding to the topography on the land surface. The difference between two bathymetric surveys conducted at different times provides the variation of the depth profile, that is the differential displacement that occurred from the initial to the final time. Bathymetric surveys are powerful tools to monitor the subsidence of the seafloor over large areas due to the production of fluids from offshore reservoirs (e.g. Ottemöller et al. (2005); De Paulis et al. (2011)). These data are acquired from a moving ship using a multi-beam echosounder system, which emits sound waves and measures the travel time that the wave takes to bounce off the seabed and return back to a receiver. Travel time data are then processed to produce maps of the water depth over the area covered by the survey. In the case of the *Maja* reservoir, bathymetric data have been collected both at the start and at the end of gas field operations. Multi-beam acquisitions have provided a map of the seafloor subsidence caused by gas production over 10 years as shown in Fig. 5. For confidentiality reasons, the contour lines are normalised to the measured peak value, u_{max}.

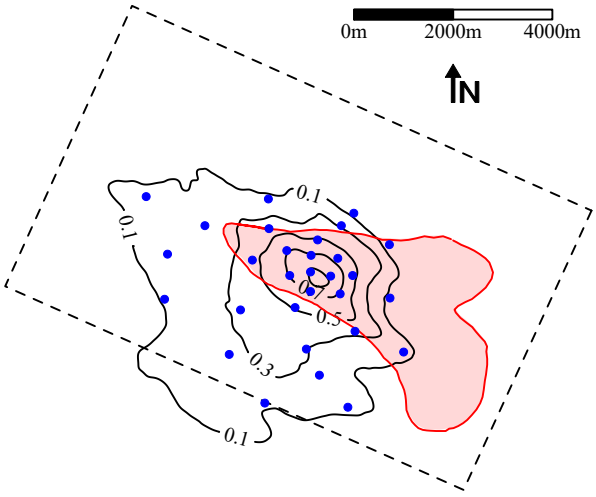

Figure 5. Subsidence contour-lines derived from multi-beam bathymetric surveys over the *Maja* gas field. The measured values are normalized to the value of the maximum displacement, u_{max}. The trace of the gas reservoir is highlighted by red color while the dashed rectangle refers to the one in Fig. 2. The blue dots are the assimilation data points.

2.4 Data Assimilation Framework

DA methods aim at constraining the forecast solution of a mathematical model based on spatio-temporal observations collected from the response of a dynamical system. Including the observations from past and present times into a simulation model allows for reducing uncertainties in the system forecast. DA application to geophysical models in atmospheric and oceanographic sciences dates back only a few decades (Burgers et al. 1998; Evensen 1994, 2003; Evensen & van Leeuwen 2000). In most applications, DA involves the use of algorithms derived from the Kalman Filter theory (Kalman 1960), such as the Ensemble Kalman Filter (EnKF) (Evensen 1994). The EnKF is a DA method in which system observations are integrated into the response of a simulator sequentially, that is, as they become available in time. The EnKF relies on a two-step forecast-update process. The forecast step relies on the solution of the forward model equations with a Monte Carlo simulation, which accounts for the uncertainty on model inputs, such as stress terms and system parameters. In the update step, the system state variables are statistically conditioned in order to resemble the available system observations.

DA gained attention in reservoir simulation in the early 2000s, as it became clear it could be used to reduce uncertainties on model parameters based on observations of the system, that is, as stochastic inverse modeling tool. A complete review of the application of DA techniques in petroleum engineering is given in Aanonsen et al. (2009).

2.4.1 The Ensemble Smoother

In this work, the ES is used for reservoir inverse modelling. The ES relies on a forecast-update process similar to the EnKF, yet the system observations at different times are assimilated all at once, as opposed to sequentially. As such, the ES is able to condition system states at all times and invariant model parameters with a single forecast-update sequence. Here, we present a brief review of the ES using the Bayesian formalism introduced by van Leeuwen and Evensen (1996).

Assume $\boldsymbol{u}$, $\boldsymbol{\alpha}$ and $\boldsymbol{d}$ as the aleatory variables representing the predicted data, the model parameters and the set of available measurements, respectively. The ES scheme is derived from Bayes' rule and the concept of conditional probability. The joint probability distribution function (PDF) of the model state and parameters conditional to the available dataset, $f\left[(\boldsymbol{u},\boldsymbol{\alpha})|\boldsymbol{d}\right]$, is given by

$$f[(\boldsymbol{u},\boldsymbol{\alpha})|\boldsymbol{d}] = \frac{f[(\boldsymbol{u},\boldsymbol{\alpha})]f[\boldsymbol{d}|(\boldsymbol{u},\boldsymbol{\alpha})]}{f(\boldsymbol{d})} \tag{2}$$

In Eq.(2), $f[(\boldsymbol{u},\boldsymbol{\alpha})]$ is the joint PDF of the model prediction and parameters, $f\left[\boldsymbol{d}|(\boldsymbol{u},\boldsymbol{\alpha})\right]$ is the PDF of the data given the model states, also know as likelihood function, and $f(\boldsymbol{d})$ is a normalisation factor. Using Bayes' rule, Eq. (2) can be rewritten as

$$f[(\boldsymbol{u},\boldsymbol{\alpha})|\boldsymbol{d}] \propto f(\boldsymbol{\alpha})f(\boldsymbol{u}|\boldsymbol{\alpha})f[\boldsymbol{d}|(\boldsymbol{u},\boldsymbol{\alpha})] \tag{3}$$

In the ES formulation, $\boldsymbol{u}$ is a vector including the predicted data $\boldsymbol{u}_1, ..., \boldsymbol{u}_K$ at a given number K of time steps, whereas the vector $\boldsymbol{d}$ is formed by the system observations $\boldsymbol{d}_1, ..., \boldsymbol{d}_J$ at a subset of J time steps ($J \leq K$). Assuming both model and measurement as first-order Markov processes, Eq. (3) can be expanded to

$$f[(\boldsymbol{u}_1, ..., \boldsymbol{u}_k, \boldsymbol{\alpha})|(\boldsymbol{d}_1, ..., \boldsymbol{d}_J)] \propto f(\boldsymbol{\alpha}) \prod_{i=1}^{K} f(\boldsymbol{u}_i|\boldsymbol{u}_{i-1}, \boldsymbol{\alpha}) \prod_{j=1}^{J} f[\boldsymbol{d_j}|(\boldsymbol{u}_{i(j)}, \boldsymbol{\alpha})] \tag{4}$$

In a linear Gaussian framework, the left-hand side of Eq.(4) is also Gaussian and the variance minimizing solution equals the maximum likelihood estimate (Evensen & van Leeuwen 2000). In particular, the ES updating equation for a parameter estimation problem is well known and reads:

$$\boldsymbol{\alpha}^a = \boldsymbol{\alpha}^f + \mathbf{C}^f_{U\Psi}\left(\mathbf{C}^f_{UU} + \mathbf{C}_{\epsilon\epsilon}\right)^{-1}\left(\boldsymbol{z} - \boldsymbol{u}^f\right) \tag{5}$$

where $\boldsymbol{\alpha}^f$ and $\boldsymbol{\alpha}^a$ are the parameters vectors prior and after the assimilation of measurements, i.e., the forecast and the update ensembles, respectively. $\mathbf{C}^f_{U\Psi}$ is the cross-covariance between the prior parameter vector $\boldsymbol{\alpha}^f$ and predicted data $\boldsymbol{u}^f$, $\mathbf{C}^f_{uu}$ is the covariace of the predicted data $\boldsymbol{u}^f$, and $\mathbf{C}_{\epsilon\epsilon}$ is the measurement error covariance matrix. The vector $\boldsymbol{z}$ holds the observations of the predicted data perturbed with an error sampled from a Gaussian PDF with zero mean and variance σ^2_ϵ.

2.5 Parameter Uncertainty and Heterogeneity

Preliminary FE geomechanical simulations indicate that the land subsidence estimated using the constitutive law shown in Fig. 3 is significantly lower than the differential bathymetric observations (Fig. 5). The reasons why this happens are possibly twofold. One is a local departure of the $c_M(\sigma_z)$ constitutive law with respect to the basin-scale average estimated by Baù et al. (2002). Another is a reservoir scale heterogeneity of c_M. To verify these hypotheses a multiplier f_{c_M} of the c_M constitutive model of Fig. 3 is introduced. The importance of heterogeneity is addressed by comparing two conceptual models, termed CM1 and CM2, which are described in the following.

2.5.1 Conceptual Model 1 (CM1)

In CM1, c_M varies initially with respect to the depth z but is horizontally constant. f_{c_M} is thus a spatially constant random variable, which is sampled from a prior PDF in order to generate the ensemble necessary to run the geomechanical model forecast. In this case, a uniform PDF within the range 1-10 is selected:

$$f_{c_M} \sim U[1, 10] \tag{6}$$

The limits of this PDF are determined after preliminary geomechanical simulations that indicate the selected range is likely to include the f_{c_M} values needed for the simulated land subsidence values to be of the same order of magnitude of the available observations. Note that f_{c_M} is applied only within the regions of the geomechanical model domain where the variations of pressure occur (Fig. 4b). The horizontal trace including these regions is depicted in Fig. 6a,b. The cumulative distribution function (CDF) of the prior ensemble for f_{c_M} is shown in Fig. 7. The CDF is approximately linear and departure from linearity is due to the finite size of the ensemble, n_{MC}=100.

2.5.2 Conceptual model 2 (CM2)

In CM2, the initial c_M is heterogenous both vertically and horizontally. Vertical variability is the same as in CM1, whereas the horizontal one is explained by assigning f_{c_M} as a two dimensional random process. The ensuing conceptual model is intended to better match the observed land subsidence distribution (Fig. 5) by accounting for the geological structure of the *Maja* reservoir, which is strongly compartmentalized (Figs. 1,2).

As for CM1, f_{c_M} is applied to the regions of the geomechanical model including pools A, B, and C (Fig. 4b). Fig. 6c shows the compartmentalization adopted in CM2. The subdomain is partitioned into seven zones based on the distribution of sealing faults and thrusts detected from 3D seismic data. The traces of these zones are shown in Fig. 6(c). f_{c_M} is uniform in each zone, but varies from one

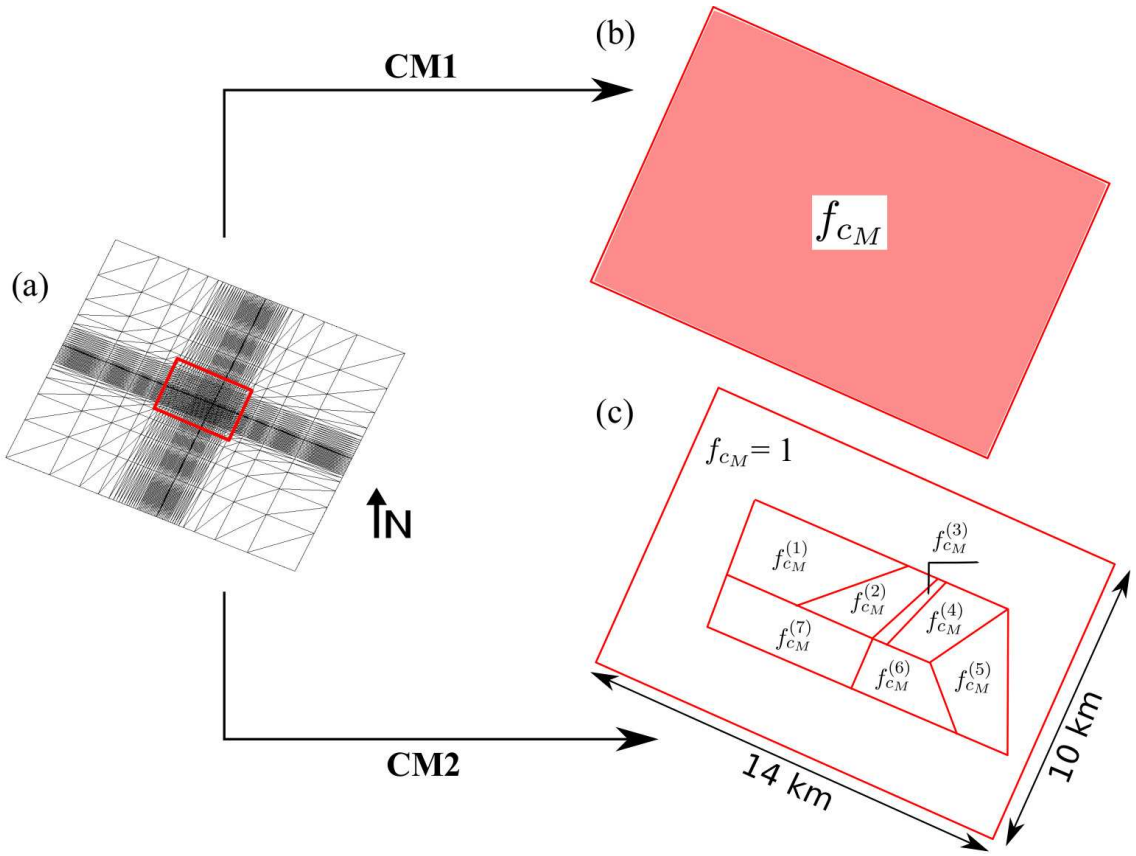

Figure 6. (a) 2D view of the geomechanical model grid (see Fig. 4(a)), (b) f_{c_M} distribution in CM1 (single random variable), and (c) $f_{c_M}^{(i)}$ distribution in CM2 within the reservoir blocks (seven random variables).

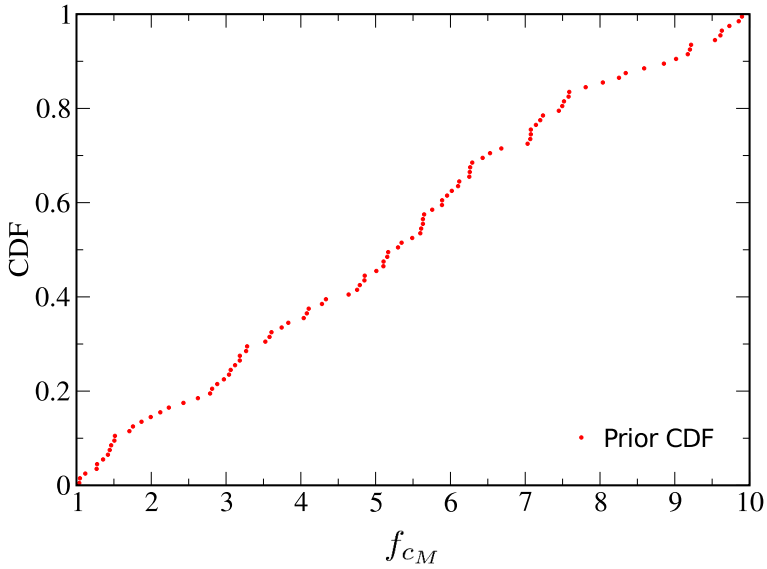

Figure 7. Prior sample Cumulative Distribution Function (CDF) of f_{c_M} (CM1).

to another. In practice, f_{c_M} is modeled as a random process characterized by seven random variables ($f_{c_M}^{(1)}$,$f_{c_M}^{(2)}$,...,$f_{c_M}^{(7)}$), each of which is sampled from a uniform PDF within the range 1-10:

$$f_{c_M}^{(i)} \sim U[1,10] \qquad i = 1,2,...,7 \tag{7}$$

The CDFs of the model parameters $f_{c_M}^{(i)}$ ($i = 1,2,...,7$) are similar to the one of Fig. 7 (n_{MC}=100). No spatial correlation is hypothesized for the $f_{c_M}^{(i)}$ variables, thus they are considered as statistically independent. The mean $\mu_{f_{c_M}}$ and the standard deviation $\sigma_{f_{c_M}}$ of the ensemble approximate with reasonable accuracy the respective theoretical vales of 5.5 and 2.6 for the uniform PDF $U[1,10]$.

3 RESULTS

In this section, the forecast of the vertical displacements obtained with the Monte Carlo geomechanical simulations and the parameter updating via the ES algorithm are described in detail for both conceptual models 1 and 2. Furthermore, the updating of the seabed subsidence is carried out with the calibrated multiplier f_{c_M} as constrained in the analysis step.

3.1 Homogeneous f_{c_M} (CM1)

The forecast Monte Carlo geomechanical simulation is run using a prior ensemble of f_{c_M} realizations, whose CDF is shown in Fig. 7. The results of this simulation are summarized in Fig. 8, which shows the maps of the mean $\mu_{v,prior}$ (subpanel a), and the coefficient of variation $C_{v,prior}$ (subpanel b) of the vertical surface displacement field at the end of the ten-year reservoir production life. Note that $\mu_{v,prior}$ is normalized to u_{max}. $C_{v,prior}$ provides an estimate of the variability of the ensemble.

The comparison of the observed land subsidence (Fig. 5) and $\mu_{v,prior}$ (Fig. 8a) is shown in Fig. 9. The simulated peak displacement value is slightly shifted to the west and the extent of the simulated subsidence bowl is significantly larger than the observed one. Consequently, the $\mu_{v,prior}$ largely over-estimates the measured subsidence over the reservoir area. A $C_{v,prior}$ of about 24% is found over the central portion of the simulated area with a progressive decrease toward the outer regions of the domain.

Parameter updating is performed by assimilation of data from the bathymetric survey. The full dataset consists of 1110 measurements of vertical surface displacement over the reservoir area, which are interpolated to obtain the map given in Fig. 5. However, only the subset of 30 observations at the locations shown in Fig. 5 is used for parameter estimation. These data points are chosen such that their interpolation over the domain resembles with sufficient accuracy the subsidence map obtained with the full dataset.

Two scenarios A and B are investigated, which differ with respect to the value of σ_ϵ assigned to the

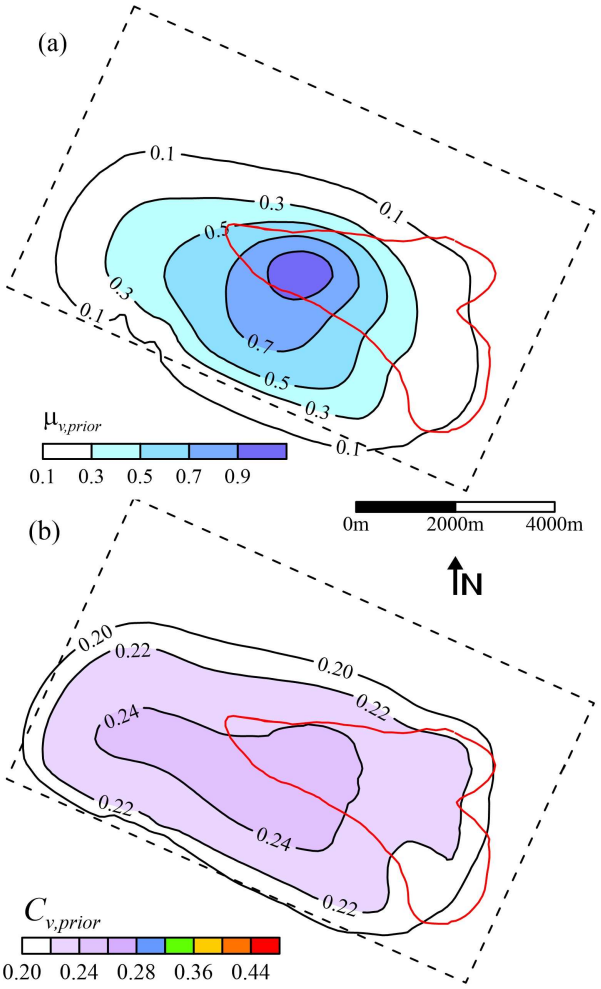

Figure 8. CM1: forecast ensemble of the seabed subsidence over the reservoir domain in terms of (a) mean, $\mu_{v,prior}$, normalized to u_{max}, and (b) coefficient of variation, $C_{v,prior}$. The trace of the gas reservoir is marked by the red line.

measurement error. In scenario A, a value $\sigma_\epsilon^{(A)}$= 0.0625 is assumed for all data. This value is deemed representative of the accuracy of the bathymetric measurements. In this scenario, all observations are given the same weight in the assimilation.

In scenario B, $\sigma_\epsilon^{(B)}$ is spatially variable in relation to the distance of the measurement points from the location where the the maximum displacement u_{max} has been observed. In particular, $\sigma_\epsilon^{(B)}$ is assigned a value of 0.025 at the seabed subsidence peak and a value of 0.125 at the farthest location, where the subsidence is smaller and the measurements considered more uncertain. All other data points are characterized by a $\sigma_\epsilon^{(B)}$ value computed by linear interpolation between the two endpoints in relation to the radial distance from the location of the subsidence peak. In this scenario, measurements away from the centre of the subsidence bowl are given a lower weight than those closer to the

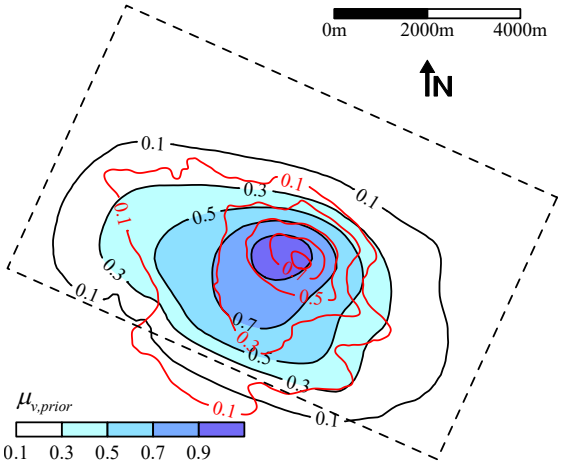

Figure 9. CM1: comparison between the measured subsidence (red contour-lines) and the mean of the forecast subsidence, $\mu_{v,prior}$, (Fig. 8a).

displacement peak. Fig. 10 shows the measurement error PDFs for the representative measurement points P_1, P_2 and P_3.

The results of the calibration are summarized in Fig. 11, which shows the posterior CDFs for f_{c_M} in both scenarios A and B. The prior CDF of f_{c_M} (Fig. 7) is also included for direct comparison. A drastic reduction in the parameter uncertainty, as explained by the spread of the sample CDF, is achieved by assimilating vertical displacements from the time-lapse bathymetric surveys. One could observe, however, that the results of scenarios A and B differ, with the updated CDF in scenario A completely to the left of the CDF in scenario B. This a direct consequence of the assigned measurement

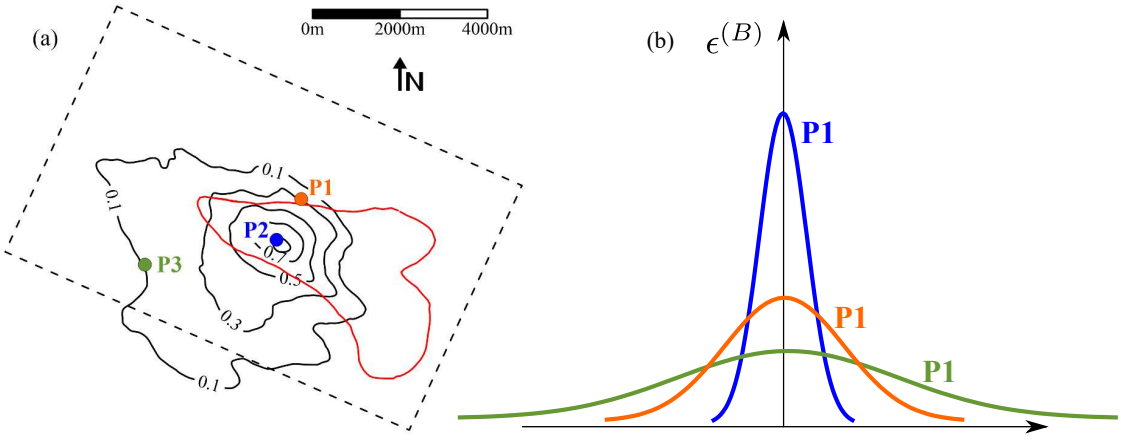

Figure 10. (a) Bathymetric map (Fig. 5) with the location of points P1, P2, and P3 used to exemplify the error distribution in scenario B (CM1). (b) PDFs of the measurement errors at P1, P2 and P3: $\epsilon^{(B)} \sim \mathcal{N}[0, \sigma_\epsilon^{(B)}]$ grows as the point distance increases from the centre of the subsidence bowl.

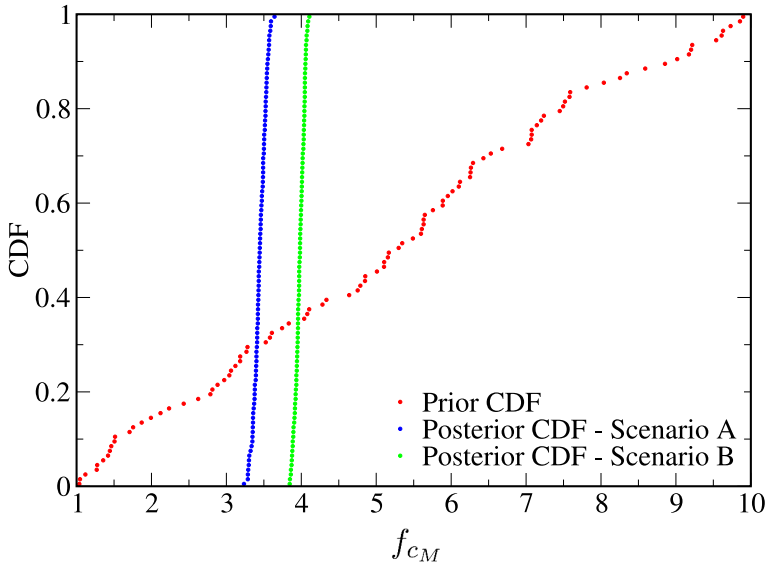

Figure 11. CM1: prior and posterior CDFs of the updating model parameter f_{c_M} for scenario A and B.

errors. In scenario A, all data carry the same weight in the assimilation, and the ES produces an updated ensemble for f_{c_M} that attempts to honor all observations regardless the displacement intensity. In scenario B, a larger weight is given to larger vertical displacements and the ES yields an ensemble of higher f_{c_M} values that tends to honor more larger displacement observations, at the center of the subsidence bowl, and less lower displacement observations at the margins of the reservoir.

These results imply that the updated f_{c_M} ensemble in scenario A leads to a narrower land subsidence bowl (in a probabilistic sense), which tends to underestimate the observed larger displacements in order to honor also the lower displacements. On the other hand, the land subsidence bowl in scenario B is wider (in a probabilistic sense) and better matches the observed larger displacements, whereas the displacements observed toward the margins of the reservoir are likely overestimated.

To confirm these hypotheses, the updated f_{c_M} ensembles are used to run a "posterior" geomechanical simulations. Fig. 12(a) and 12(b) show the profiles of the seafloor subsidence mean after ten-years of gas production obtained for scenarios A and B and compared to the bathymetric observations. As expected, increasing the mean value of the multiplier f_{c_M} from scenario A to scenario B yields:

(i) a reduction of the maximum subsidence underestimate;

(ii) an enlargement of the subsidence bowl.

These contrasting effects suggest that a better match of the observations cannot be achieved assuming f_{c_M} as a single random variable within the whole model. These results point to the use of a spatial variablity of f_{c_M}, as previously discussed in Section 2.5.2.

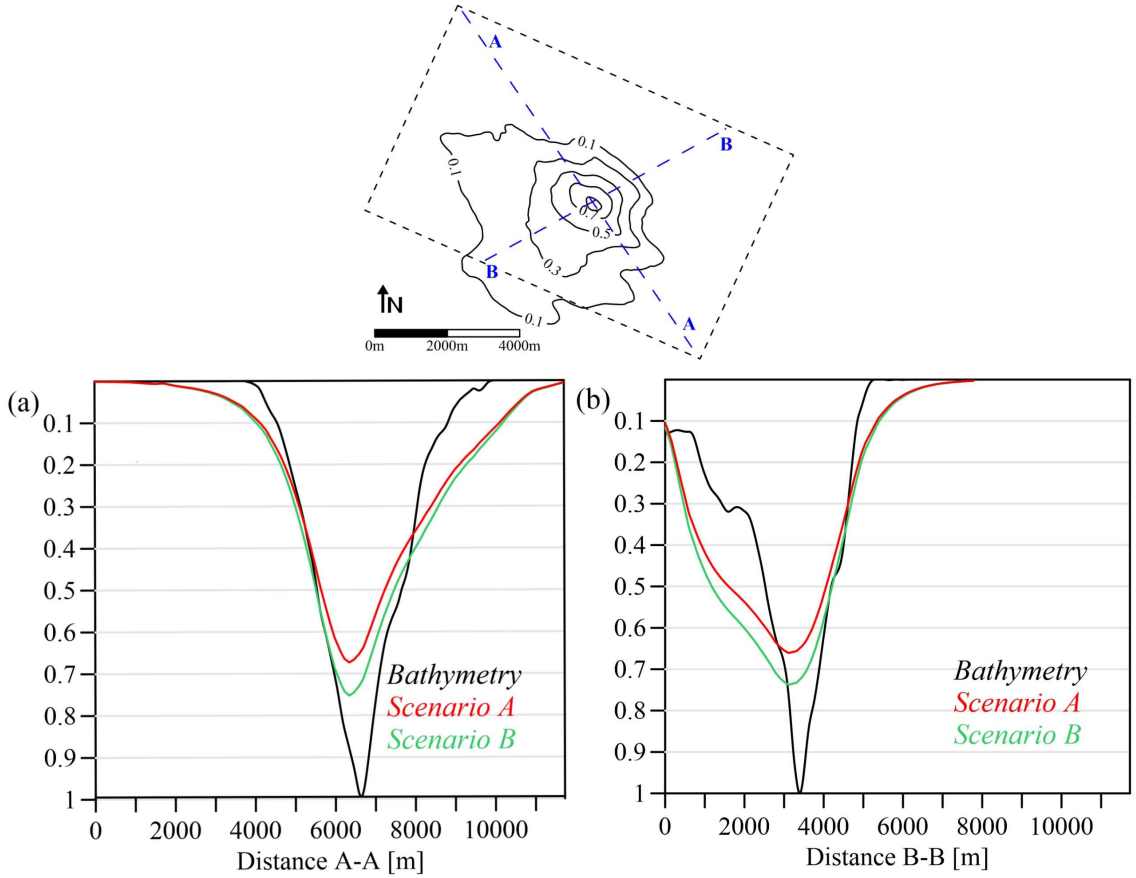

Figure 12. CM1: profiles of the mean seabed subsidence $\mu_{v,post}$ along (a) section A-A and (b) section B-B traced on the top map. Scenario A and B are compared with the bathymetric profile. Note that the subsidence values are normalized to u_{max}.

3.2 Heterogeneous f_{c_M} (CM2)

The prior ensemble of heterogeneous f_{c_M} realizations, generated as in Section 2.5.2, is run to from the forecast ensemble of the surface vertical displacements over the geomechanical model domain. As in CM1, the simulation spans the ten-year production period and the ensemble size n_{MC} equals 100. The results of the forecast Monte Carlo simulation are summarized in Fig. 13, which shows the maps of the mean and the coefficient of variation of the surface vertical displacement. The peak subsidence value from the forecast ensemble mean is equal to $1.01u_{max}$. The comparison of Fig. 8a and Fig. 13a indicates that CM1 and CM2 produce similar outcomes in terms of forecast seabed subsidence mean. By contrast, the coefficient of variation takes on higher values with CM2 (Fig. 13b) than with CM1 (Fig. 8b).

Fig. 13b points out that the pattern of $C_{v,prior}$ resembles the hypothesized spatial distribution of f_{c_M} shown in Fig. 6, which relies on the compartmentalization of the reservoir. Moreover, Fig. 13b shows that the statistical variability of surface displacement is more pronounced over the zones charac-

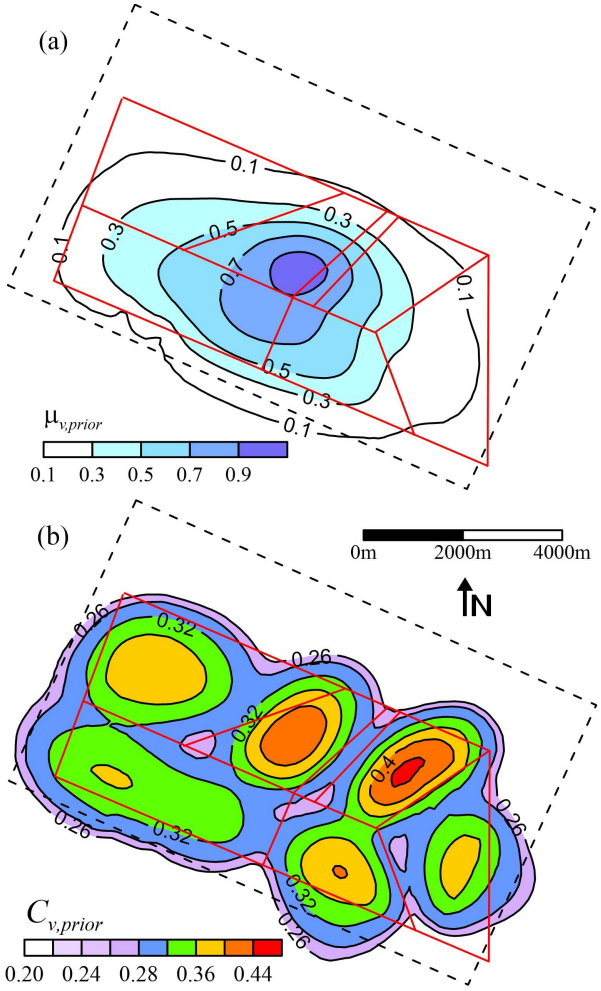

Figure 13. CM2: maps of (a) the mean and (b) the coefficient of variation of the forecast ensemble of seabed subsidence over the reservoir domain. The mean values are scaled to the maximum measured vertical displacement.

terized by larger areal extent and higher values of ΔP. In particular, $C_{v,prior}$ reaches maximum values of 0.43 and 0.45 in zones 2 and 4, respectively, whereas in zones 1, 5, 6, and 7 it is not exceed 0.36.

For CM2, the update step is carried out similarly to CM1, except that seven f_{c_M} parameters - as opposed to one - are estimated by inverting the vertical displacement measured over the 30 locations shown in Fig. 5. In this case, the standard deviation of the measurement error σ_ϵ is assumed uniformly distributed for all measurements and equal to 0.0625. The results from the ES are presented in Fig. 14a and Table 1. Fig. 14a shows the posterior CDFs for the f_{c_M} value in the seven zones shown in Fig. 6. The prior CDF of f_{c_M} (Fig. 7) is also included for direct comparison. Table 1 reports the major statistics of the updated f_{c_M} ensembles in the seven reservoir zones.

The ES has the effect of steering the f_{c_M} ensembles toward different values in the seven zones charactering CM2, which are somehow quantified by the mean and the median of the updated ensem-

Table 1. Statistics from the posterior $f_{c_M}^{(i)}$ ensembles. Note that the mean $\mu_{f_{c_M}}$ and the standard deviation $\sigma_{f_{c_M}}$ of the prior ensemble are equal to 5.5 and 2.6, respectively.

zone #	mean $\mu_{f_{c_M}}$	median m_{c_M}	std. dev. $\sigma_{f_{c_M}}$
1	3.05	2.91	0.89
2	3.59	3.58	0.28
3	9.67	9.57	1.14
4	2.02	2.08	0.64
5	2.92	2.77	1.65
6	2.69	2.66	0.50
7	1.46	1.47	0.51

bles (Table 1). Fig. 14a shows that the spread of the posterior CDF of f_{c_M} is shrunk significantly for all zones with respect to the prior CDF. The $\sigma_{f_{c_M}}$ values given in Table 1 indicate that the spread varies significantly among zones. The largest value of $\sigma_{f_{c_M}}$ is found in zone 5, the easternmost in Fig. 6. The contribution to the surface displacements from the deep deformation of block 5 is likely less significant than for the other blocks because the pressure variation ΔP is relatively smaller. Indeed, the constraint of $f_{c_M}^{(5)}$ is more difficult to obtain.

Table 1 shows that for all zones the median and the mean of the updated parameter ensemble are very similar, which indicates that the posterior PDFs are reasonably symmetric. The updated means $\mu_{f_{c_M}}$ are typically lower than the mean (5.5) of the prior ensembles, except for zone 3 where such mean equals 9.67. This value almost exceeds the upper support value of the prior PDF $U[1, 10]$ (Eq. 7). Thus, the ES analysis suggests that higher values for $f_{c_M}^{(3)}$ are required to match the measured seafloor settlement. Moreover, the posterior PDF is quite spread around the mean value indicating that this parameter is hardly constraint by the ES. Indeed, zone 3 is rather small and the model response is not sufficiently affected by the variation of the $f_{c_M}^{(3)}$ values. The largest reduction of the ensemble spread is achieved for zone 2.

The updated parameter ensemble is used to run the posterior geomechanical simulations and the map of the mean of the surface displacement after ten-years of gas production is shown in Fig. 14b. The extent of the seabed subsidence bowl is smaller than that shown in the profiles of Fig. 12 for CM1. In the next section this different is further discussed.

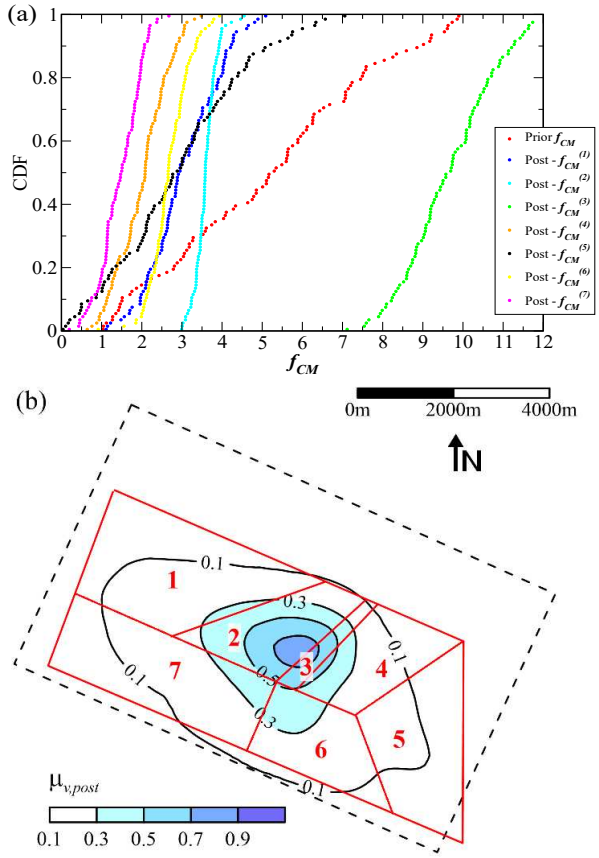

Figure 14. CM2: (a) posterior CDFs of the random variables $f_{c_M}^{(i)}$ after assimilation of vertical displacements data and (b) updated subsidence map after ten-year of gas production using the calibrated $f_{cM}^{(i)}$ and normalized to u_{max}.

4 DISCUSSION

Fig. 15 summarizes, in quantitative terms, the effectiveness of the ES procedure for the two conceptual models addressed in this study. The figure shows maps of the percentage error, calculated as $\delta = 100 \times (u_{meas} - u_{sim})/|u_{meas}|$, where u_{meas} and u_{sim} are the measured and simulated surface vertical displacements over the reservoir domain. Figs. 15a and 15b relate to CM1, for scenarios A and B, respectively. Figs. 15c relates to CM2. Positive δ values indicate model underestimation, i.e., the simulated displacements smaller than the observations.

Scenarios A and B (CM1) are characterized by similar spatial distributions of δ. The average percentage error, μ_δ equals -36% in scenarios A and -51% in scenario B. The standard deviation σ_δ is 51% and 57% in A and B, respectively. Negative δ is observed in the majority of the mapped region showing that CM1 leads to generally overestimating the seabed subsidence. By distinction, positive δ

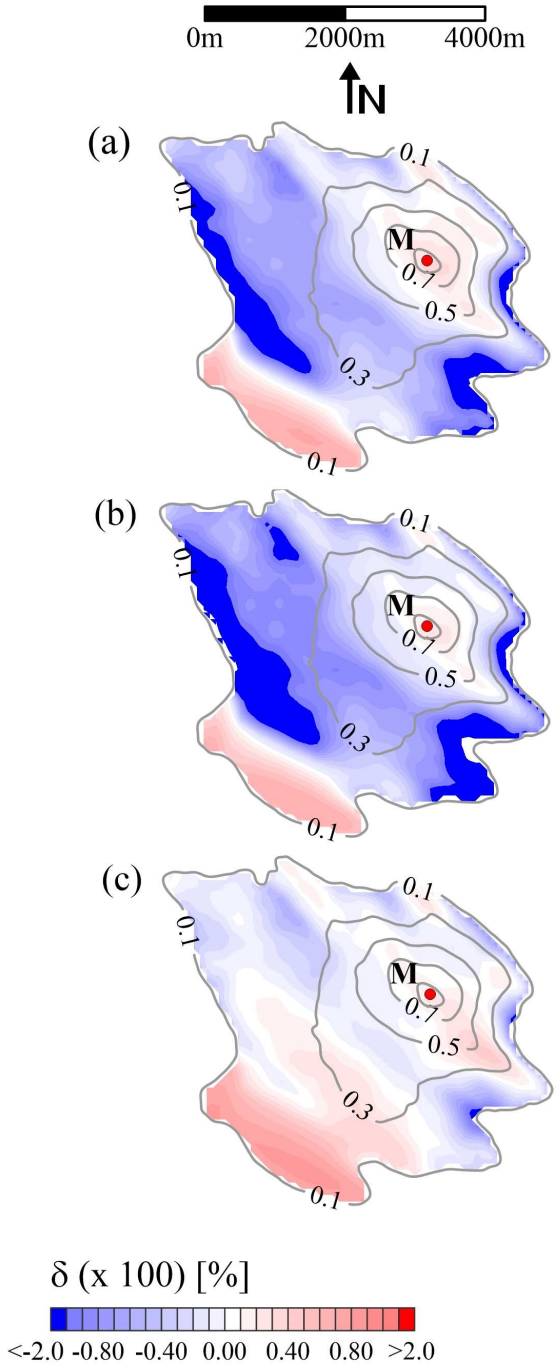

Figure 15. Distribution of the percentage error δ over the area with measured subsidence larger than 0.1 for (a) CM1-Scenario A, (b) CM1-Scenario B, and (c) CM2. Positive (red) and negative (blue) values are representative of a model underestimation and overestimation, respectively. The black contour-lines provide the normalized measured subsidence (Fig. 5).

values are located in the areas where the measured subsidence is greater than about 0.6. In particular, at the location where the largest surface displacement has been observed (point M in Fig. 15), values of +34% and +26% are found in scenario A and B, respectively.

Adopting model CM2, the spatial distribution of δ results much less variable than in the case of CM1 (Fig. 15c). The values of μ_δ and σ_δ are equal to +4% and 32%, respectively. At point M, the model underestimation reduces to +22% thus indicating that an higher f_{c_M} in this area may help to improve the misfit between simulation and observations. However, the overestimation over the aquifer obtained with CM1 is almost removed by adopting CM2.

The comparison of the maps in Fig. 15 clearly points out that CM2 allows for a significantly improved matching of the observed surface displacements with respect to CM1. The less constraints are prescribed to the model, i.e., a c_M heterogeneous distribution, the better the model solution adapts to the observed response. However, the enlargement of the parameter space may lead to run a too large number of Monte Carlo simulations to adequately sample the posterior PDFs. Indeed, the model parametrization is crucial, in particular in real applications where an high computational cost is required for each model run. In this sense, the previous knowledge from the geological structure of the reservoir, such as the compartmentalization derived from the presence of sealing faults/thrusts, may help improving the characterization of the field.

5 CONCLUSIONS

The ES algorithm provides an efficient tool for reservoir parameter estimation using observations of seafloor subsidence, i.e., vertical displacements measured through time-lapse bathymetric surveys. These data represent a significant indirect information of the rock formation properties. In particular, the ES allows for the characterization of the reservoir vertical uniaxial compressibiltiy, c_M, namely the geomechanical parameter that mostly controls the reservoir compaction due to the pore pressure depletion during fluid production. The method is herein tested on a real offshore gas reservoir with a highly complex distribution of sealing faults and thrusts that are also used to characterize the geomechanical properties of the reservoir. The major conclusions can be summarized as follows:

(i) data of seafloor displacements can be helpful to derive the mechanical properties of a gas reservoir;

(ii) weighting their observations based on the reliability affects the outcome of the updating scheme;

(iii) using the reservoir geologic structure may improve the reservoir characterization;

(iv) the ES constrains the prior PDF of the heterogeneous geomechanical parameters in the portions

of the reservoir contributing considerably to the observed subsidence, e.g., where the pressure change and the compacting volume are significant;

(v) the assumption of a heterogeneous parametrization for the compressibility, i.e., a different value of c_M, in each reservoir block may provide a better matching of the seafloor subsidence compared to the case of a uniform c_M.

Further improvements will focus on the validation of the above results using different data sources including compaction measurements from RMT. Moreover, the compressibility law could be revisited in light of the fact the only one law for the whole reservoir may not prove satisfactory results to address the local reservoir geomechanical behaviour.

ACKNOWLEDGMENTS

This research was supported by ENI E&P through a three-year project "*Data Assimilation in Geomechanics*" carried out at the University of Padua in parternship with the Colorado State University.

REFERENCES

Aanonsen, S., Nævdal, G., Oliver, D., Reynolds, A. C., & Vallès, B., 2009. The Ensemble Kalman Filter in Reservoir Engineering – A Review. *SPE J*, **14**(3), 393–412.

Baù D., Gambolati, G. & Teatini, P., 2000. Residual land subsidence near abandoned gas fields raises concern over Northern Adriatic coastland. *EOS Trans. AGU*, **81**(22), 245-249, and, *Earth in Space*, **13**(1), 9-13.

Baù D., Ferronato, M., Gambolati, G. & Teatini, P., 2002. Basin scale compressibility of the Northen Adriatic by the radioactive marker technique. *Geotechnique*, **52**, 605–616.

Baù, D., Ferronato, F., Gambolati, G., Teatini, P., & Alzraiee, A., 2015. Ensemble smoothing of land subsidence measurements for reservoir geomechanical characterization. *Int. J Numer. Anal. Meth. Geomech.*, **39**, 207–228.

Bouttier, F., Courtier, P., 1999. Data assimilation concepts and methods. *Meteorological training course lecture series. ECMWF*, 1–58.

Burgers, G., van Leeuwen, P. J., Peter & Evensen, G., 1998. Analysis Scheme in the Ensemble Kalman Filter. *Monthly Weather Review*, **126**, 1719–1724.

Cassiani, G., & Zoccatelli, C., 2000. Subsidence risk in venice and nearby areas, Italy, owing to offshore gas fields: A stochastic analysis. *Environmental & Engineering Geoscience*, **6**, 115–128.

De Waal, J.A., Roest, J.P.A., Fokker, P.A., Kroon, I.C., Breunese, J.N., Muntendam-Bos, A.G., Oost, A.P. & van Wirdum, G., 2012. The effective subsidence capacity concept: How to assure that subsidence in the Wadden Sea remains within defined limits? *Netherlands Journal of Geosciences*, **91-3**, 385–399.

Emerick, A. A., Reynolds, A. C., 2013. Ensemble smoother with multiple data assimilation. *Computers & Geosciences*, **55**, 3–15.

Evensen G., 1994. Sequential data assimilation with non linear quasi-geostrophic model using Monte-Carlo methods to forecast error statisticsi. *J. geophys. Res.,* , **55**(C5), 343–367.

Evensen, G., & van Leeuwen, P. J., 2000. An Ensemble Kalman Smoother for Nonlinear Dynamics. *Monthly Weather Review*, **128**, 1852–1867.

Evensen, G., 2003. The Ensemble Kalman Filter: Theoretical formulation and practical implementation. *Ocean Dynamics*, **53**, 343–367.

Ferronato, M., Gambolati, G., Teatini, P., & Baù, D., 2004. Interpretation of radioactive marker measurements to evaluate compaction in the Northern Adriatic gas fields. *SPE Journal of Reservoir Evaluation and Engineering*, **6**, 401–411.

Ferronato, M., Gambolati, G., Teatini, P., & Baù, D., 2004. Radioactive marker measurements in heterogeneous reservoirs: numerical study. *International Journal of Geomechanics*, **4**, 79–92.

Ferronato, M., Castelletto, N., Gambolati, G., Janna, C., Teatini, P., 2013. II cycle compressibility from satellite measurements. *Geotechnique*, **63**, 479–486.

Fokker, P. A., Wassing, B. B. T., van Leijen, F. J., Hanssen, R. F., & Nieuwland, D. A., 2013. Data Assimilation of PS-InSAR Movement Measurements Applied to the Bergermeer Gas Field. *International Workshop on Geomechanics and Energy*.

Fredrich, J. T., Arguello, L. G., Deitrick, G. L., & de Rouffignac, E. P., 2000. Geomechanical modeling of reservoir compaction, surface subsidence, and casing damage at the Belridge diatomite field. *SPE Reserv. Eval. Eng.*, **3**, 348–359.

Gambolati, G., Ferronato, M., Teatini P., Deidda, R., & Lecca, G., 2001. Finite element analysis of land subsidence above depleted reservoirs with pore pressure gradient and total stress formulations. *International Journal for Numerical and Analytical Methods in Geomechanics*, **25**, 307–327.

Geertsma, J., 1973. A basic theory of subsidence due to reservoir compaction: the homogeneous case. *Verhandelingen Kon. Ned. Geol. Mijnbouwk. Gen.*, **28**, 43–62.

Gu, Y., Oliver, D. S., 2005. History matching of the PUNQ-S3 reservoir model using the Ensemble Kalman Filter. *SPE J*, **10**(2), 51–65.

Hatchell, P. & Bourne, S., 2005. Rocks under strain: Strain-induced time-lapse time shifts are observed for depleting reservoirs. *The Leading Edge*, **24**(12), 1222–1225. doi: 10.1190/1.2149624

Herwanger, J.V. & Horne, S. A., 2009. Linking reservoir geomechanics and time-lapse seismics: Predicting anisotropic velocity changes and seismic attributes. *Geophysics*, **74**(4), W13–W33.

Hilbert L. B., Gwinn R. L., Moroney T. A., Deitrick G. L., 2005. Field-scale and wellbore modeling of compaction-induced casing failures. *SPE Journal of Drilling & Completion 1999*, textbf14(2), 92–101.

Hueckel, T., Cassiani, G., Prvost, J. H. & Walters, D. A., 2005. Field derived compressibility of deep sediments of Northern Adriatic. *Proceedings of Seventh International Symposium on Land Subsidence*, Shanghai, China, Special Volume, F.B.J. Barends et al. (eds.), 35–50.

Janna, C., Castelletto, N., Ferronato, M., Gambolati, G., & Teatini, P., 2012. A geomechanical transversely isotropic model of the Po River basin using PSInSAR derived horizontal displacement. *International Journal*

of Rock Mechanics and Mining Sciences, **51**, 105–118.

Jolley, S. J., Fisher, Q. J. & Ainsworth, R. B., 2010. Reservoir compartmentalization: an introduction. *Geological Society, London, Special Publications*, textbf347, 1–8.

Kalman, R. E., 1960. A new approach to linear filtering and prediction problems. *Transaction of ASME - Journal of Basic Engineering*, **82** (Series D), 35–45.

Kristiansen, T.G. & Plischke, B., 2010. History matched full field geomechanics model of the Valhall Field including water weakening and re-pressurasation. *SPE*, 131505.

Lorentzen, R. J., Nævdal, G., & Lage, A. C. V. M., 2003. Tuning of parameters in a two-phase flow model using an Ensemble Kalman Filter. *International Journal of Multiphase Flow*, **29**(8), 1283–1309.

Mezghani, M., Fornel, A., Langlais, V., & Lucet, N., 2004. History matching and quantitative use of 4D seismic data for an improved reservoir characterization. *SPE Annual Technical Conference and Exibition, 26-29 September, Houston, Texas*.

Morton, R. A., Bernier, J. C., & Barras, J. A., 2006. Evidence of regional subsidence and associated interior wetland loss induced by hydrocarbon production, Gulf Coast region, USA. *Environ Geol*, **50**: 261–274, DOI 10.1007/s00254-006-0207-3.

Nævdal, G., Johnsen, L. M., Aanonsen, S. I., & Vefring, E., 2003, Reservoir monitoring and continuous model updating using the ensemble Kalman filter. *SPE Annual Technical Conference and Exhibition* (SPE 84372).

Ottemöller, L., Nielsen, H. H., Atakan, K., Braunmiller, J., & Havskov, J., 2005. The 7 May 2001 induced seismic event in the Ekofisk oil field, North Sea. *J. Geophys. Res.*, **110**, B10301.

De Paulis, R., Prati, C., Scirpoli, S., Rocca, F., Tesei, A., Sletner, A., Biagini, S., Guerrini, P., Gasparoni, F., Carmisciano, C., & Locritani, M., 2011. SAS multipass interferometry for monitoring seabed deformation using a high-frequency imaging sonar. *IEEE Xplore*, 10.1109/Oceans-Spain.2011.6003448.

Sayers, C., den Boer, L., Hooyman, P., & Lawrence, R., 2006. Predicting reservoir compaction and casing deformation in deepwater turbidities using a 3D mechanical earth model. *SPE*, 103926, DOI: 10.2118/103926-MS.

Skjervheim, J.–A., Evensen, G., Hove, J., & Vabø, J. G., 2011. An Ensemble Smoother for assisted History Matching. *SPE Reservoir Simulation Symposium*, (SPE 141929).

Teatini, P., Castelletto, N., Ferronato, M., Gambolati, G., Janna, C., Cairo, E., Marzorati, D., Colombo, D., Ferretti, A., Bagliani, A., & Bottazzi, F., 2011. Geomechanical response to seasonal gas storage in depleted reservoirs: A case study in the Po River basin, Italy. *Journal of Geophysical Research - Earth Surface*, **116**, F02002.

van Hasselt, J. P., 1992. Reservoir compaction and surface subsidence resulting from oil and gas production. *Geol. Mijnbouw*, **71**, 107–118.

van Leeuwen, P. J., & Evensen, G., 1996. Data Assimilation and Inverse Methods in Terms of a Probabilistic Formulation. *Mon. Wea. Rev.*, **124**, 2898–2913.

Zoccarato, C., Baù D., Ferronato, M., Gambolati, G., Alzraiee, A., & Teatini, P., 2016. Data assimilation of surface displacements to improve geomechanical parameters of gas storage reservoirs. *Under review, JGR:*

Solid Earth.